



Cite this: *Nanoscale Adv.*, 2021, **3**, 1962

## Carbon-coated $\text{Fe}_3\text{O}_4$ core–shell superparamagnetic nanoparticle-based ferrofluid for heat transfer applications†

Mohd Imran, <sup>a</sup> Nasser Zouli, <sup>a</sup> Tansir Ahamad, <sup>b</sup> Saad M. Alshehri, <sup>b</sup> Mohammed Rehaan Chandan, <sup>\*c</sup> Shahir Hussain, <sup>d</sup> Abdul Aziz, <sup>e</sup> Mushtaq Ahmad Dar <sup>f</sup> and Afzal Khan <sup>\*g</sup>

Herein, we report the investigation of the electrical and thermal conductivity of  $\text{Fe}_3\text{O}_4$  and  $\text{Fe}_3\text{O}_4@\text{carbon}$  ( $\text{Fe}_3\text{O}_4@\text{C}$ ) core–shell nanoparticle (NP)-based ferrofluids. Different sized  $\text{Fe}_3\text{O}_4$  NPs were synthesized via a chemical co-precipitation method followed by carbon coating as a shell over the  $\text{Fe}_3\text{O}_4$  NPs via the hydrothermal technique. The average particle size of  $\text{Fe}_3\text{O}_4$  NPs and  $\text{Fe}_3\text{O}_4@\text{C}$  core–shell NPs was found to be in the range of ~5–25 nm and ~7–28 nm, respectively. The thickness of the carbon shell over the  $\text{Fe}_3\text{O}_4$  NPs was found to be in the range of ~1–3 nm. The magnetic characterization revealed that the as-synthesized small average-sized  $\text{Fe}_3\text{O}_4$  NPs (ca. 5 nm) and  $\text{Fe}_3\text{O}_4@\text{C}$  core–shell NPs (ca. 7 nm) were superparamagnetic in nature. The electrical and thermal conductivities of  $\text{Fe}_3\text{O}_4$  NPs and  $\text{Fe}_3\text{O}_4@\text{C}$  core–shell NP-based ferrofluids were measured using different concentrations of NPs and with different sized NPs. Exceptional results were obtained, where the electrical conductivity was enhanced up to ~3222% and ~2015% for  $\text{Fe}_3\text{O}_4$  (ca. 5 nm) and  $\text{Fe}_3\text{O}_4@\text{C}$  core–shell (ca. 7 nm) NP-based ferrofluids compared to the base fluid, respectively. Similarly, an enhancement in the thermal conductivity of ~153% and ~116% was recorded for  $\text{Fe}_3\text{O}_4$  (ca. 5 nm) and  $\text{Fe}_3\text{O}_4@\text{C}$  core–shell (ca. 7 nm) NPs, respectively. The exceptional enhancement in the thermal conductivity of the bare  $\text{Fe}_3\text{O}_4$  NP-based ferrofluid compared to that of the  $\text{Fe}_3\text{O}_4@\text{C}$  core–shell NP-based ferrofluid was due to the more pronounced effect of the chain-like network formation/clustering of bare  $\text{Fe}_3\text{O}_4$  NPs in the base fluid. Finally, the experimental thermal conductivity results were compared and validated against the Maxwell effective model. These results were found to be better than results reported till date using either the same or different material systems.

Received 21st January 2021  
Accepted 6th February 2021

DOI: 10.1039/d1na00061f  
[rsc.li/nanoscale-advances](http://rsc.li/nanoscale-advances)

## 1. Introduction

The dispersion of nanoparticles (NPs) in various fluids enhances their thermal conductivity, which have potential application in heat transfer as coolants in various systems such as automobile radiators, refrigerators, process engineering systems, electronic devices, solar energy heaters, pulsating pipes, and thermosyphons.<sup>1–5</sup> There are several typical base fluids used for heat transfer applications such as water, ethylene glycol, ethanol, methanol, dimethyl formamide, poly-alfaolefin, and oils.<sup>6–13</sup> Ferrofluids or magnetic fluids are stable colloidal homogeneous suspensions of magnetic NPs (~10 nm in diameter) in an aqueous or a non-aqueous carrier liquid.<sup>14</sup> The dispersion of NPs in these base fluids results in the formation of a nanofluid, and if NPs are magnetic in nature, the resulting fluid is termed a ferrofluid. Generally, NPs show enhanced electrical, thermal, optical and mechanical properties because of their large surface to volume ratio.<sup>15–17</sup> Magnetic NPs such as  $\text{Fe}_3\text{O}_4$  have attracted great interest from the scientific community because of their unique properties such as

<sup>a</sup>Department of Chemical Engineering, Faculty of Engineering, Jazan University, P.O. Box 706, Jazan 45142, Saudi Arabia

<sup>b</sup>Department of Chemistry, College of Science, King Saud University, P.O. Box 2455, Riyadh 11451, Saudi Arabia

<sup>c</sup>Colloids and Polymers Research Group, School of Chemical Engineering, Vellore Institute of Technology, Vellore, Tamilnadu 632014, India. E-mail: chandan1816@gmail.com; Tel: +91-04162202668

<sup>d</sup>Department of Electrical Engineering, Faculty of Engineering, Jazan University, P.O. Box 706, Jazan 45142, Saudi Arabia

<sup>e</sup>Department of Mechanical Engineering, Faculty of Engineering, Jazan University, P.O. Box 706, Jazan 45142, Saudi Arabia

<sup>f</sup>Center of Excellence for Research in Engineering Materials, College of Engineering, King Saud University, Riyadh, 11421, Kingdom of Saudi Arabia

<sup>g</sup>State Key Laboratory of Silicon Materials, School of Materials Science and Engineering, Zhejiang University, Hangzhou 310027, China. E-mail: afzalkhan@zju.edu.cn; Tel: +86-15669097732

† Electronic supplementary information (ESI) available. See DOI: [10.1039/d1na00061f](https://doi.org/10.1039/d1na00061f)



biocompatibility, high electrochemical response and thermal stability.<sup>18</sup> Consequently,  $\text{Fe}_3\text{O}_4$  NP-based ferrofluids exhibit enhanced thermal and electrical conductivities.<sup>19–21</sup> However, NPs have high surface energy, which results in their agglomeration or settling at the bottom of the dispersion liquid when used for a long period. Therefore, the coating of inorganic or organic materials over  $\text{Fe}_3\text{O}_4$  NPs is necessary for their good dispersion and long-term stability.<sup>18</sup> The oxidation of magnetite ( $\text{Fe}_3\text{O}_4$ ) NPs leads to the formation of a stable phase of iron oxide, which is  $\gamma\text{-Fe}_2\text{O}_3$  NPs (maghemite), and a more stable form, *i.e.*,  $\alpha\text{-Fe}_2\text{O}_3$  (hematite) under particular conditions.<sup>22</sup> Therefore, it is necessary to protect superparamagnetic  $\text{Fe}_3\text{O}_4$  NPs from physical and chemical changes by encapsulating them with other materials. Accordingly, capping  $\text{Fe}_3\text{O}_4$  NPs with another sub-material (shell) can result in their good dispersion and stability, as reported by Sharma *et al.*<sup>18</sup> Hence, various core-shell NPs have been reported thus far, especially  $\text{Fe}_3\text{O}_4@\text{C}$  core-shell NPs, for *e.g.*, Xuan *et al.* synthesized carbon-encapsulated  $\text{Fe}_3\text{O}_4$  core-shell particles *via* the reduction of glucose.<sup>23</sup> Conversely, Wang *et al.* synthesized single carbon layer-coated ultra-small  $\text{Fe}_3\text{O}_4$  NPs using a one-step hydrothermal technique for surface-enhanced Raman spectroscopy studies,<sup>24</sup> and He *et al.* used *in situ*-synthesized carbon-encapsulated  $\text{Fe}_3\text{O}_4$  NPs as an anode material for lithium ion batteries.<sup>25</sup> Moreover, Zhao *et al.* employed the hydrothermal method for the synthesis of interconnected carbon nanospheres covering  $\text{Fe}_3\text{O}_4$  NPs.<sup>26</sup> Similarly, Liang *et al.* synthesized  $\text{Fe}_3\text{O}_4@\text{Au}$  core-shell NPs for the ultrasensitive detection of carbohydrate–protein interactions.<sup>27</sup> A magnetic metal nanocomposite was coated by carbon to prepare  $\text{FeNi}@\text{C}$  core-shell NPs.<sup>28</sup> Li *et al.* synthesized  $\text{Cu}@\text{C}$  core-shell NPs *via* a simple state reduction method and investigated their optical properties.<sup>29</sup> Similarly,  $\text{Ag}@\text{C}$  core-shell NPs were synthesized *via* the wet chemical route and catalysed under hydrothermal conditions, which exhibited hydrophilic and unique optical properties.<sup>30</sup> Moreover, the reverse micelle method was employed to prepare  $\text{Fe}@\text{Fe-oxide}$  and  $\text{Fe}@\text{Au}$  core-shell nanostructures.<sup>31,32</sup> These core-shell NPs possessed an added advantage over other NPs as their shell can protect their core from physical and chemical changes. Thus, biocompatible, highly reactive and toxic NPs can be covered with biologically compatible, non-reactive and environmentally friendly materials in the form of shells.

To further explore the unique properties of core-shell NPs, they were introduced in a dispersion liquid to make stable ferrofluids for various applications. Recently, ferrofluids were prepared by dispersing  $\text{Fe}_3\text{O}_4$  NPs in mineral oil and  $\gamma\text{-Fe}_2\text{O}_3$  NPs in various base fluids.<sup>19–21</sup> Their thermal conductivities were enhanced multiple folds compared to that of the base liquids. Similarly, Cui *et al.* synthesized superparamagnetic  $\text{Fe}_3\text{O}_4$  NPs, which were dispersed in perfluoropolyether base fluid, and the resulting ferrofluid exhibited enhanced viscosity and thermal conductivity.<sup>33</sup> Zupan *et al.* prepared a ferrofluid by dispersing iron(II,III) oxide NPs in water for heat transfer application.<sup>34</sup> Furthermore,  $\text{Fe}_3\text{O}_4$  NPs were dispersed in water and a maximum 200% enhancement in thermal conductivity was observed.<sup>35</sup>

Core-shell NP-based ferrofluids also exhibit good biocompatibility and improved properties. Accordingly, the other applications of core-shell NP-based ferrofluids include multimodal imaging, hyperthermia, drug delivery, cytocompatibility, tumour targeting, cancer chemotherapy and thermotherapy and other possible biological applications.<sup>36–38</sup> Similarly, magnetic NP systems are widely used in the MRI-guided delivery of magneto-electric drug nano-carriers to the brain.<sup>39</sup> Magneto-electric core-shell NPs exhibit enhanced cell uptake and control drug release under the influence of an applied and magnetic field.<sup>40</sup> To manage central nervous system (CNS) diseases, surface-engineered magnetic NPs have been employed as a tool *via* image-guided therapy and theranostics.<sup>41</sup> Magneto-electric NPs (MENPs) are stimulus-responsive nanosystems for controlled drug release and cell uptake.<sup>42,43</sup> The futuristic application of these magnetic core-shell nanostructures may be projected in the biomedical field, where previous studies showed the use of magnetic core-shell nanoparticles as an antimicrobial agent.<sup>44</sup> Targeted drug delivery and drug delivery to the brain are limited due to their complicated methods and structural behavior. Thus, to achieve this goal, magnetic core-shells have been suggested as important nanocarriers.<sup>45,46</sup>

Although nanofluids based on non-magnetic NPs are widely studied, to date, few studies investigating the thermal conductivity of magnetic core-shell NPs for heat transfer applications have been performed.<sup>47–49</sup> To the best of our knowledge, the electrical and thermal conductivities of superparamagnetic  $\text{Fe}_3\text{O}_4@\text{C}$  core-shell NPs have rarely been reported. Therefore, herein, we synthesized  $\text{Fe}_3\text{O}_4$  NPs using a chemical co-precipitation method followed by the hydrothermal synthesis technique, which led to the formation of  $\text{Fe}_3\text{O}_4@\text{C}$  core-shell NPs. Furthermore, these NPs were characterized using various techniques and their electrical and thermal conductivities were measured. The super-paramagnetic  $\text{Fe}_3\text{O}_4@\text{C}$  core-shell NPs exhibited good thermal and electrical properties, and thus can be exploited for heat transfer applications, such as cooling of electronic devices, fuel cells, and solar cells.<sup>50</sup>

## 2. Experimental

### 2.1. Materials and methods

Ferrous sulphate heptahydrate ( $\text{FeSO}_4 \cdot 7\text{H}_2\text{O}$ ), ferric chloride hexahydrate ( $\text{FeCl}_3 \cdot 6\text{H}_2\text{O}$ ) and sodium hydroxide ( $\text{NaOH}$ ) were purchased from Sigma Aldrich. Absolute alcohol and hydrochloric (HCl) acid were procured from Chem-Lab (Belgium) and Scharlau (Spain), respectively. All chemicals were of research grade and used without further purification. Similarly, fructose of analytical grade was purchased from Gem-Chem (India) and used as received. Deionized (DI) water obtained from an ultrapure water unit (Puris-Expe water system) was used during the synthesis of the  $\text{Fe}_3\text{O}_4$  NPs.

### 2.2. Synthesis of $\text{Fe}_3\text{O}_4$ NPs

$\text{Fe}_3\text{O}_4$  NPs were synthesized *via* a chemical co-precipitation method. In a typical co-precipitation method, 0.32 mol of ferrous sulphate heptahydrate ( $\text{FeSO}_4 \cdot 7\text{H}_2\text{O}$ ) and 0.64 mol of



ferric chloride were dissolved in 100 mL DI water separately. The  $\text{Fe}^{2+}/\text{Fe}^{3+}$  ions were mixed properly before dispersing them in an alkali solution. The ion mixture was then transferred to a 100 mL burette. In a 250 mL round-bottom flask, 1.5 M NaOH solution was prepared and the volume was made up to 100 mL. The iron salt ions were then added dropwise to the above alkali solution under vigorous stirring. The pH of the solution was maintained at around 11–12 during the reaction. An additional amount of NaOH solution could be added to the reaction vessel if needed. As soon as the iron salts were added to the alkali solution, precipitation of the salts started, resulting in the formation of a black-colored co-precipitate. The precipitate was then stirred for 30 min at room temperature. Subsequently, the solution was allowed to settle for 30 min and with the help of a strong magnet, the precipitate was separated from the unreacted solution. Finally, the obtained precipitate was washed several times with distilled water. Similarly, by tuning the pouring of aqueous solution of iron salt (drops) into the aqueous solution of alkali and stirring rate,  $\text{Fe}_3\text{O}_4$  NPs with three different sizes were obtained including 5 nm, 12 nm and 25 nm.

### 2.3. Synthesis of $\text{Fe}_3\text{O}_4@\text{C}$ core–shell NPs

The as-synthesized  $\text{Fe}_3\text{O}_4$  NPs of different sizes were dispersed separately in a 5 M aqueous solution of glucose and kept in a tight capped 500 mL bottle, which was half-filled with the solution. To coat a carbon shell over the  $\text{Fe}_3\text{O}_4$  NPs, the sample solution was shaken properly and then left in an autoclave for 4–5 h at high pressure and 180 °C. The carbonization of glucose occurred at 180 °C during the hydrothermal treatment. After this reaction, the system was allowed to cool to room temperature. A dark black-colored solution smelling like sugarcane vinegar was obtained, which was decanted with the help of a strong magnet. Subsequently, the sample was washed with distilled water several times. Finally, the black-colored precipitate was collected and dried at 80 °C for 4–5 h in an oven.<sup>18,23</sup> Consequently,  $\text{Fe}_3\text{O}_4@\text{C}$  core–shell NPs with different sizes including 7 nm, 14 nm and 28 nm were obtained using this technique.

### 2.4. Preparation of ferrofluids

We introduced fine powders of  $\text{Fe}_3\text{O}_4$  and  $\text{Fe}_3\text{O}_4@\text{C}$  core–shell NPs into DI water in separate beakers. Given that the NPs were highly magnetic in nature, the mixtures were sonicated for 3–4 hours for better dispersion of the NPs. Eventually, we obtained a highly monodispersed NP solution. The prepared ferrofluids were found to be stable without any external applied magnetic field for a long time. Before their application in a heat exchanger, the ferrofluids were sonicated again for better heat transfer results. Different concentrations of ferrofluids were prepared in a similar way for heat transfer and electrical conductivity measurements.

### 2.5. Characterization

The phase and crystallinity of the as-synthesized  $\text{Fe}_3\text{O}_4$  and  $\text{Fe}_3\text{O}_4@\text{C}$  powder samples were identified by XRD (D8  $\text{A}\alpha\text{S}$

Advance X-ray diffractometer using  $\text{Cu K}\alpha$  radiation,  $\lambda = 1.54156 \text{ \AA}$ ). Raman analyses were conducted using a Raman spectrometer (Aramis LabRam spectrometer). The microstructure analyses of the as-synthesized powders were carried out using a transmission electron microscope (TEM) (JEOL, JEM2100F) operated at 200 kV. X-ray photoelectron spectroscopy (XPS) was performed for elemental information using an X-ray photoelectron spectrometer (Thermo Fisher, USA). Moreover, the functional groups were identified using FT-IR (ATR-FT-IR Nicolet iS 10). The magnetic properties of the as-synthesized powders were analyzed using an ADE 3473-70 Technologies vibrating sample magnetometer (VSM) in the range of  $-10 \text{ kOe}$  to  $10 \text{ kOe}$  with a magnetization error of  $\pm 1\%$ . The zeta potential values of the prepared ferrofluids were obtained using a Zetasizer (Nano-ZS; Malvern, UK) operated at room temperature. The electrical conductivities of the ferrofluids were measured using an HI 2300 NaCl/TDS/EC meter (HANNA Instruments). For the measurement of the thermal conductivity of the ferrofluids with different concentrations, a WL-373 (GUNT Hamburg, Germany) instrument was used. This unit is particularly suited for the determination of the coefficients of thermal conduction of liquids and gaseous materials. The unit was comprised of a double-walled cylinder with an integrated heater acting as the heat source, and the surrounding cylinder as the heat sink. There was a narrow slot in the unit, which was sufficient to prevent heat by convection, and therefore the heat of transfer in the slot is due to the thermal conduction. Due to the constant width of the slot, thermal conduction occurs in a plane wall. The heat transferred,  $Q$ , can be calculated using Fourier's law as follows:

$$Q_a = \frac{\lambda \times \Delta T \times A}{\delta} \quad (1)$$

where  $Q_a$  = heat transfer,  $\lambda$  = thermal conductivity coefficient,  $\Delta T$  = temperature gradient,  $A$  = surface area and  $\delta$  = thickness of the slot.

## 3. Results and discussion

Fig. 1a and b show the XRD patterns of the as-synthesized  $\text{Fe}_3\text{O}_4$  powder and  $\text{Fe}_3\text{O}_4@\text{C}$  powder samples, respectively. Fig. 1a shows diffraction peaks at  $2\theta$  values of around 30.09°, 35.45°, 43.02°, 53.59°, 57.20° and 62.72°, which correspond to the (220), (311), (400), (422), (511) and (440) crystal planes, respectively. The peak positions and relative intensities of the  $\text{Fe}_3\text{O}_4$  powder sample matched with the JCPDS card no. 19-629, which confirmed the crystalline nature and cubic spinel structure of the powder sample. Similarly, for the  $\text{Fe}_3\text{O}_4@\text{C}$  powder sample, the diffraction peaks at around 30.2°, 35.5°, 43.17°, 53.59°, 57.37° and 62.72° correspond to the (220), (311), (400), (422), (511) and (440) crystal planes, respectively, as shown in Fig. 1b.<sup>18,23</sup> There is a negligible shift in the diffraction peaks, which suggest that the  $\text{Fe}_3\text{O}_4$  powder sample did not transform into another iron oxide phase during the synthesis of the  $\text{Fe}_3\text{O}_4@\text{C}$  powder sample.<sup>18,23</sup> Fig. 1c and d show the FT-IR spectra of the  $\text{Fe}_3\text{O}_4$  and  $\text{Fe}_3\text{O}_4@\text{C}$  powder samples, respectively. The peaks observed at 571 and 631  $\text{cm}^{-1}$  correspond to



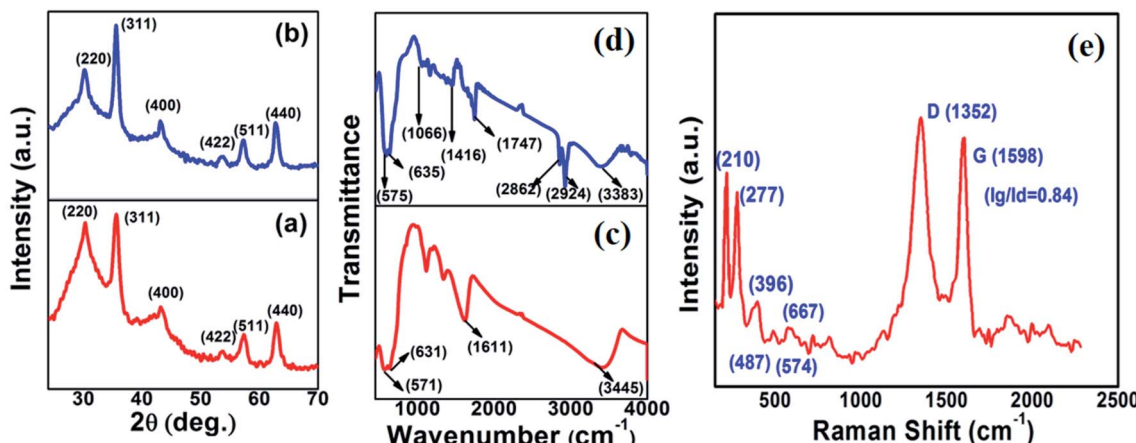


Fig. 1 XRD patterns of (a)  $\text{Fe}_3\text{O}_4$  and (b)  $\text{Fe}_3\text{O}_4@\text{C}$  core–shell NPs. FTIR spectra of (c)  $\text{Fe}_3\text{O}_4$  and (d)  $\text{Fe}_3\text{O}_4@\text{C}$  core–shell NPs and (e) Raman spectrum of  $\text{Fe}_3\text{O}_4@\text{C}$  core–shell NPs.

the vibrations of Fe–O (Fig. 1c).<sup>18,23,51</sup> However, for the  $\text{Fe}_3\text{O}_4@\text{C}$  powder sample, the Fe–O vibration bands were observed at 575 and  $635\text{ cm}^{-1}$ . The small shift in the Fe–O vibration band is due to the carbon coating over  $\text{Fe}_3\text{O}_4$ . Moreover, the decrease in the vibration frequency of the bond indicates the addition of carbon. The peaks at  $2924\text{ cm}^{-1}$  and  $2862\text{ cm}^{-1}$  refer to the C–H

stretching vibrations, and the peaks at  $1416\text{ cm}^{-1}$  and  $1066\text{ cm}^{-1}$  refer to the C–H bending vibrations and C–O stretching vibrations, respectively, for the  $\text{Fe}_3\text{O}_4@\text{C}$  NPs. The broad band observed at  $3300$ – $3450\text{ cm}^{-1}$  and the band at  $1611\text{ cm}^{-1}$  present in both spectra correspond to the O–H stretching mode and the H–O–H bending mode, respectively,

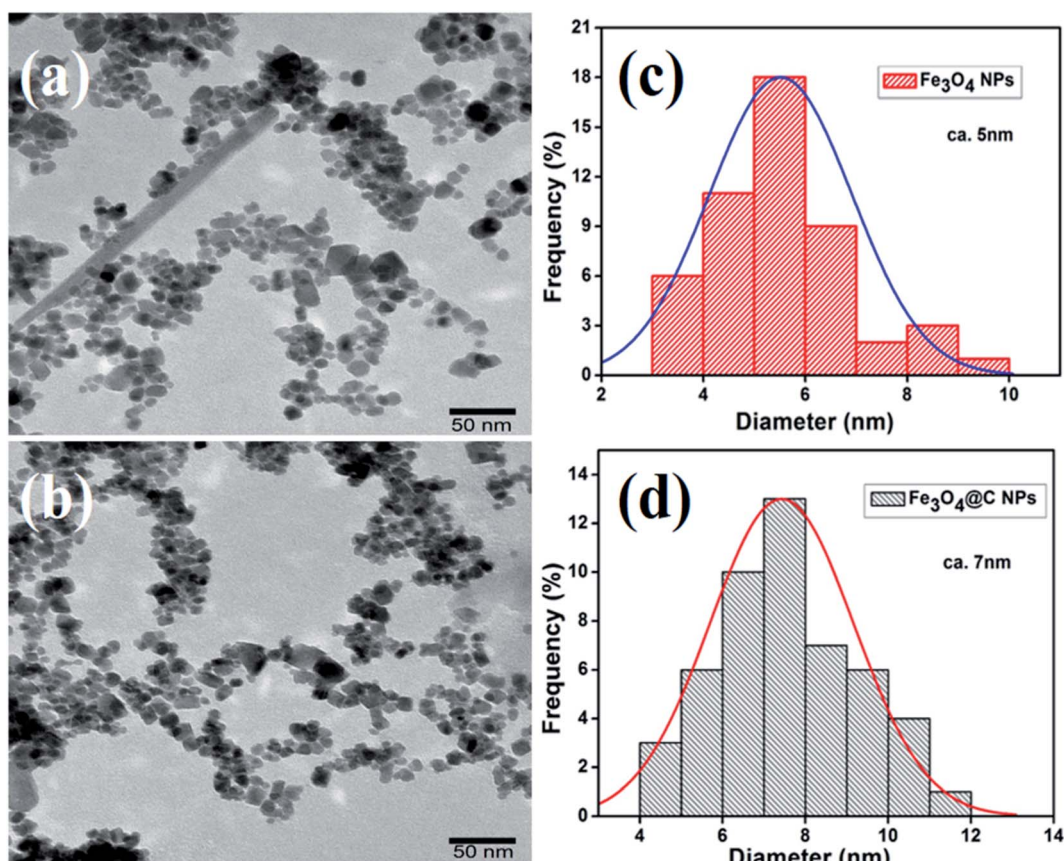


Fig. 2 Low magnification TEM images of (a)  $\text{Fe}_3\text{O}_4$  NPs (5 nm) and (b)  $\text{Fe}_3\text{O}_4@\text{C}$  core–shell NPs (7 nm) and (c) and (d) their corresponding size distribution histograms, respectively.



indicating the presence of interstitial water molecules.<sup>18,23,52</sup> The Raman spectrum of the Fe<sub>3</sub>O<sub>4</sub>@C powder sample is shown in Fig. 1e, where the intense D band and G band were observed at around 1352 and 1598 cm<sup>-1</sup>, respectively. The D band can be attributed to sp<sup>2</sup> carbon, which indicates a disordered graphitic structure and the G band can be attributed to sp<sup>3</sup> carbon. The other significant peaks at around 396 cm<sup>-1</sup> and 487 cm<sup>-1</sup> in the Raman spectrum suggest the T<sub>2g</sub> phonon vibration mode in Fe<sub>3</sub>O<sub>4</sub>.<sup>53</sup> The peaks at 574 cm<sup>-1</sup> and 667 cm<sup>-1</sup> suggest the Fe=O vibration, which is known as the A<sub>1g</sub> phonon vibration mode and generally observed due to the symmetric stretching of the O atom along the Fe–O bonds in Fe<sub>3</sub>O<sub>4</sub>.<sup>53</sup>

Fig. 2a and b show the low-magnification TEM images of the as-synthesized Fe<sub>3</sub>O<sub>4</sub> and Fe<sub>3</sub>O<sub>4</sub>@C powder samples, and their corresponding size distribution histograms are shown in Fig. 2c and d, respectively. It was observed that the as-synthesized powder samples were comprised of NPs, which were mono-dispersed on the TEM Cu grid. The average particle size of the Fe<sub>3</sub>O<sub>4</sub> NPs and Fe<sub>3</sub>O<sub>4</sub>@C NPs were found to be around 5 nm and 7 nm, respectively. Similarly, the TEM images of two different sized Fe<sub>3</sub>O<sub>4</sub> NPs (12 nm and 25 nm) and Fe<sub>3</sub>O<sub>4</sub>@C core–shell NPs (14 nm and 28 nm) together with their corresponding size distribution histograms are shown in Fig. S1 (ESI†). Fig. 3a and b show the high-magnification TEM and HRTEM images of the Fe<sub>3</sub>O<sub>4</sub> NPs, respectively. As shown in Fig. 3b, three different types of planes were identified with the *d* spacings of 0.29, 0.26 and 0.21 nm, which correspond to the (220), (311) and (400) planes of cubic Fe<sub>3</sub>O<sub>4</sub>.<sup>53</sup> The HRTEM results also confirmed the crystalline nature of the as-synthesized Fe<sub>3</sub>O<sub>4</sub> NPs and suggest that they did not transform into another stable form of iron oxide. Similarly, Fig. 3c and d show the high-magnification TEM

and HRTEM images of the carbon-encapsulated Fe<sub>3</sub>O<sub>4</sub> (Fe<sub>3</sub>O<sub>4</sub>@C) NPs, respectively. The carbon-shell coating over the Fe<sub>3</sub>O<sub>4</sub> NPs was found to be amorphous in nature, and the thickness of the carbon shell over a random Fe<sub>3</sub>O<sub>4</sub> core NP was found to be approximately in the range of 0.8–1.2 nm.

Fig. 4a shows the XPS survey scans of the bare Fe<sub>3</sub>O<sub>4</sub> NPs (red color) and Fe<sub>3</sub>O<sub>4</sub>@C core–shell NPs (black color). Three significant peaks corresponding to the Fe 2p, O 1s and C 1s core levels were obtained for the carbon-coated Fe<sub>3</sub>O<sub>4</sub> NPs, which confirmed the composition of the Fe<sub>3</sub>O<sub>4</sub>@C core–shell NPs, whereas the C 1s core level peak was missing for the bare Fe<sub>3</sub>O<sub>4</sub> NPs. Fig. 4b shows the high-resolution spectrum of Fe 2p core level, *i.e.*, Fe 2p<sub>3/2</sub> and Fe 2p<sub>1/2</sub>, which correspond to the binding energies 710.5 eV and 724.1 eV, respectively. No peak was observed at 719 eV, which corresponds to  $\alpha$ -Fe<sub>2</sub>O<sub>3</sub>, indicating that no phase transformation occurred.<sup>53</sup> Fe exists in two states, *i.e.*, Fe<sup>2+</sup> and Fe<sup>3+</sup>, in Fe<sub>3</sub>O<sub>4</sub>. The peak at 710.3 eV (pink) is attributed to the Fe<sup>2+</sup> state in Fe 2p<sub>3/2</sub>. The peak observed at 712.7 eV (purple) corresponds to the Fe<sup>3+</sup> state in Fe 2p<sub>3/2</sub>. Similarly, for Fe 2p<sub>1/2</sub>, a peak appeared at 725.7 eV (blue), which correlates to Fe<sup>3+</sup>, and another peak appeared at 723.7 eV (cyan), corresponding to Fe<sup>2+</sup>. The HR O 1s core level spectrum is shown Fig. 4c. The peaks at 531.7 eV (green) and 529.9 eV (wine) are attributed to the Fe–O bond in the Fe<sub>3</sub>O<sub>4</sub> NPs. The other peak observed at 533.1 eV (blue) corresponds to the O–H bond. The HR C 1s core level spectrum is shown in Fig. 4d. The peaks at 28.63 eV (blue) and 285.2 eV (green) correspond to the C–C sp<sup>3</sup> and C=C sp<sup>2</sup> carbon, respectively. The small peaks observed at 287.5 eV (purple) and 289.1 eV (pink) are attributed to C–O and C=O, respectively, which may originate from airborne organic contaminants. Moreover, it was also

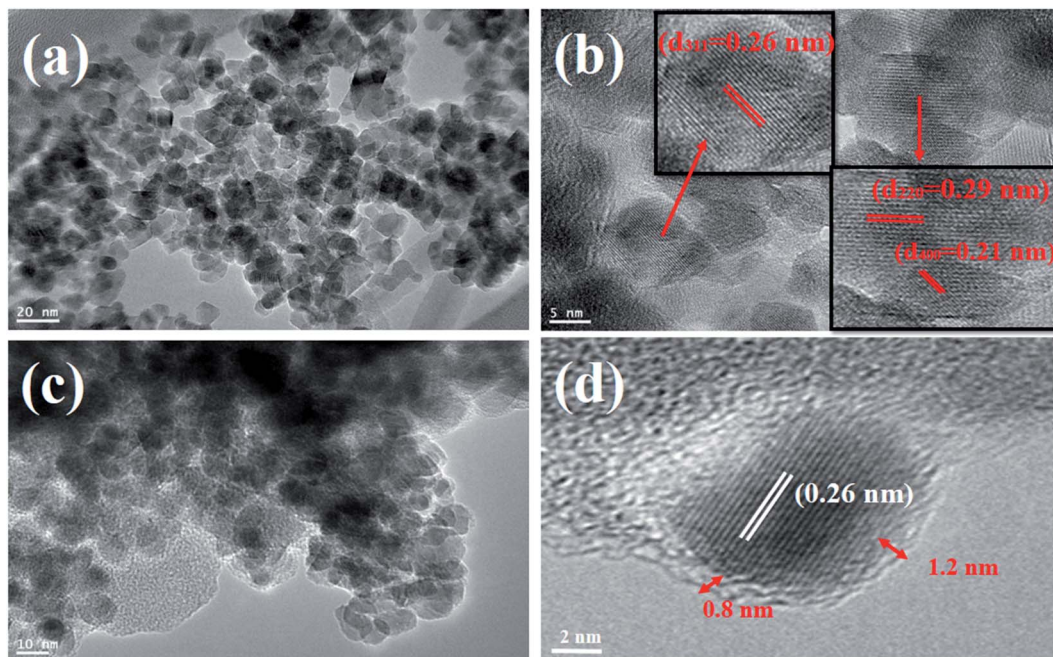


Fig. 3 High-magnification TEM images of (a) Fe<sub>3</sub>O<sub>4</sub> NPs and (c) Fe<sub>3</sub>O<sub>4</sub>@C core–shell NPs. (b) and (d) HRTEM images of Fe<sub>3</sub>O<sub>4</sub> NPs and a random Fe<sub>3</sub>O<sub>4</sub>@C core–shell NP.



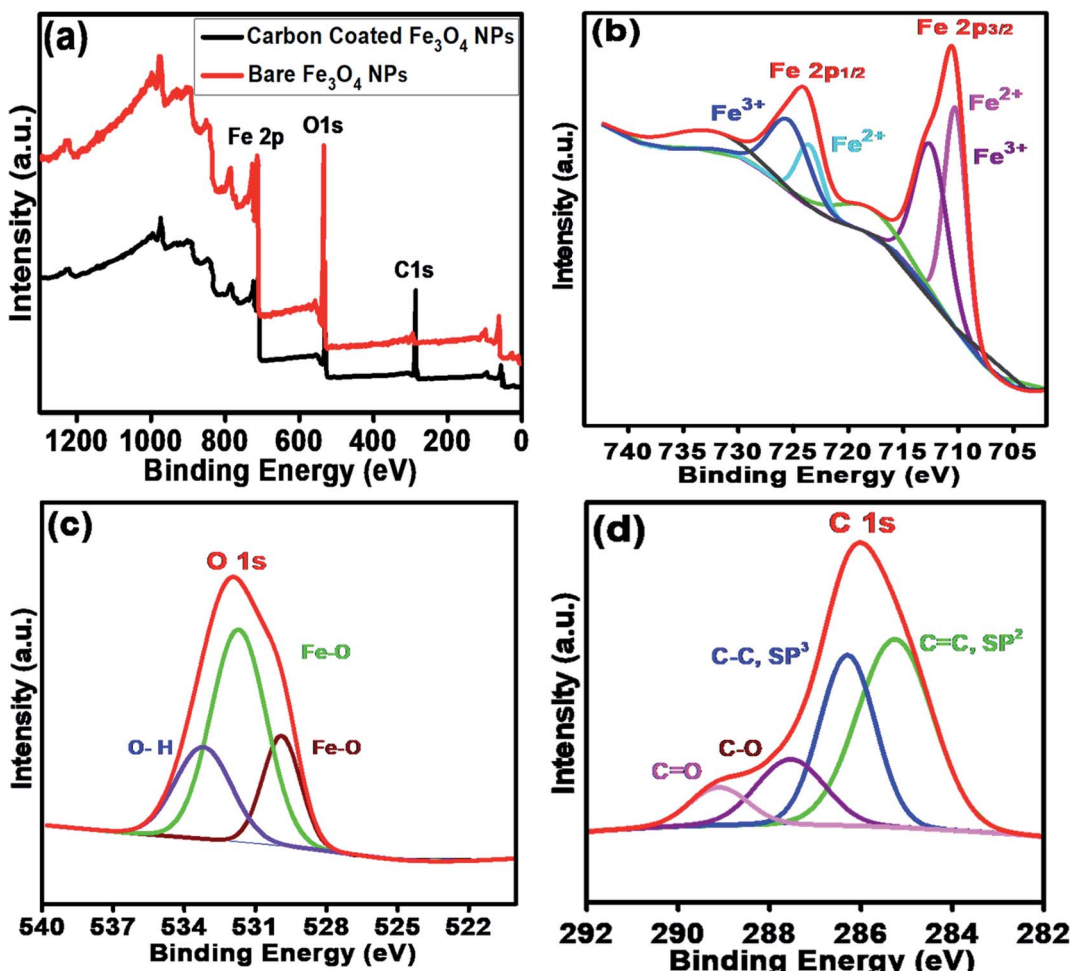


Fig. 4 (a) XPS survey scan of bare  $\text{Fe}_3\text{O}_4$  NPs and carbon-coated  $\text{Fe}_3\text{O}_4$  ( $\text{Fe}_3\text{O}_4@\text{C}$ ) core–shell NPs. HR scans of (b)  $\text{Fe} 2\text{p}_{3/2}$  and  $\text{Fe} 2\text{p}_{1/2}$  and (c) O 1s and (d) C 1s core level spectra.

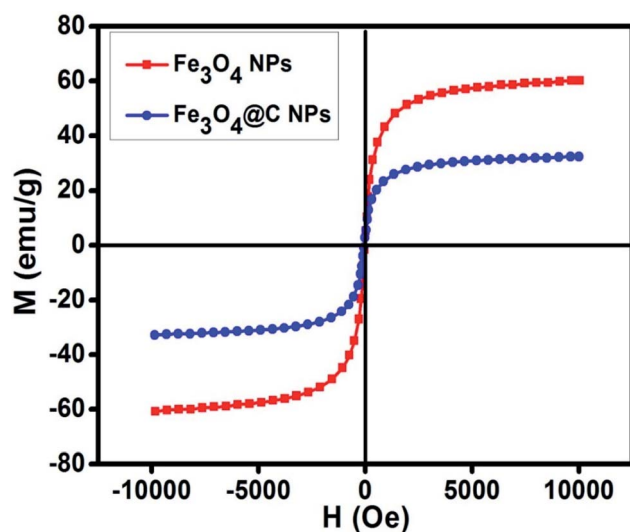


Fig. 5 Magnetic hysteresis loop of  $\text{Fe}_3\text{O}_4$  NPs (ca. 5 nm) and  $\text{Fe}_3\text{O}_4@\text{C}$  core–shell NPs (ca. 7 nm).

confirmed that no reaction between the  $\text{Fe}_3\text{O}_4$  NPs and carbon coating occurred.

Fig. 5 shows the magnetic characterization of the small average-sized  $\text{Fe}_3\text{O}_4$  NPs (ca. 5 nm) and  $\text{Fe}_3\text{O}_4@\text{C}$  core–shell NPs (ca. 7 nm) with respect to different magnetic fields at 300 K. An unusual behavior in magnetic properties was observed in NPs compared to their bulk counterpart. The magnetization was observed to be 60 emu  $\text{g}^{-1}$  for  $\text{Fe}_3\text{O}_4$  NPs (ca. 5 nm), and it was obvious that there was no coercivity and remanence. Hence, the as-synthesized  $\text{Fe}_3\text{O}_4$  NPs (ca. 5 nm) were found to be superparamagnetic in nature.<sup>24</sup> Similarly, the as-synthesized  $\text{Fe}_3\text{O}_4@\text{C}$  core–shell NPs (ca. 7 nm) also exhibited superparamagnetic behavior, and the magnetization was found to be 30 emu  $\text{g}^{-1}$  with no coercivity and remanence. The saturation magnetization was found to be much lower in the case of the core–shell NPs. The low value of the magnetic saturation may be attributed to the carbon coating over the  $\text{Fe}_3\text{O}_4$  NPs as carbon materials are diamagnetic in nature.<sup>54</sup> A low coercive field was also observed in the case of both NPs which indicate their spherical shape.<sup>55</sup> The stabilities of the prepared ferrofluids were evaluated in terms of zeta potential and the results are shown in Table 1 and Fig. 6. The zeta potentials were measured

**Table 1** Zeta potential of the different sized  $\text{Fe}_3\text{O}_4$  and  $\text{Fe}_3\text{O}_4@\text{C}$  NP-based ferrofluids at 0.7 vol% of NPs

Ferrofluid sample	Nanoparticles	Size (nm)	Zeta potential (mV)
1	$\text{Fe}_3\text{O}_4$	5	6.49
2	$\text{Fe}_3\text{O}_4$	12	-1.12
3	$\text{Fe}_3\text{O}_4$	25	-7.18
4	$\text{Fe}_3\text{O}_4@\text{C}$	7	-18.7
5	$\text{Fe}_3\text{O}_4@\text{C}$	14	-19.4
6	$\text{Fe}_3\text{O}_4@\text{C}$	28	-20.2

for the different sized  $\text{Fe}_3\text{O}_4$  and  $\text{Fe}_3\text{O}_4@\text{C}$  NP-based ferrofluids at 0.7 vol% of NPs. The results suggest coagulation/agglomeration behavior for the  $\text{Fe}_3\text{O}_4$  NP-based ferrofluids (zeta potential  $<\pm 5$ ), leading to the formation of networks, whereas the  $\text{Fe}_3\text{O}_4@\text{C}$  NP-based ferrofluids showed moderate stability ( $\pm 10 < \text{zeta potential} < \pm 30$ ).<sup>56,57</sup> An increase in the stability of NPs or their good dispersibility in the base fluid is generally observed for core–shell NPs.<sup>58,59</sup>

The electrical conductivities (ECs) of the as-synthesized  $\text{Fe}_3\text{O}_4$  NPs (*ca.* 5 nm) and  $\text{Fe}_3\text{O}_4@\text{C}$  core–shell NP (*ca.* 7 nm)-based ferrofluids with different concentrations and temperature were measured. The EC of the ferrofluid was found to increase with an increase in the concentration of both types of NPs, as shown in Fig. 7a and b. Fig. 7a shows the ECs of distilled water (base fluid) and the ferrofluids with different concentrations of  $\text{Fe}_3\text{O}_4@\text{C}$  core–shell NPs at various temperatures. The

EC of the ferrofluids was found to be many times higher than that of the base fluid. Similarly, Fig. 7b shows the ECs of  $\text{Fe}_3\text{O}_4$  NP-based ferrofluids, which followed the same trend as observed in Fig. 7a for the  $\text{Fe}_3\text{O}_4@\text{C}$  core–shell NP-based ferrofluids. However, the ECs of the bare  $\text{Fe}_3\text{O}_4$  NP-based ferrofluids were found to be higher than the core–shell NP-based ferrofluids. This may be attributed to the amorphous nature of the carbon coating, which resulted in a decrease in the EC. Fig. 7c shows a comparison of the ECs of the  $\text{Fe}_3\text{O}_4$  and  $\text{Fe}_3\text{O}_4@\text{C}$  core–shell NP-based ferrofluids at 50 °C. It was quite obvious that the  $\text{Fe}_3\text{O}_4$  NP-based ferrofluid at a particular concentration of  $\text{Fe}_3\text{O}_4$  NPs exhibited a higher EC compared to the core–shell NP-based ferrofluid. Fig. 7d demonstrates the percentage enhancement in the EC compared to that of the base fluid. It was found that the  $\text{Fe}_3\text{O}_4$  NP-based ferrofluid exhibited the highest value of EC, *i.e.*, 205  $\mu\text{S cm}^{-1}$  for 0.7 vol% of NPs at 50 °C. Conversely, the EC value of 130  $\mu\text{S cm}^{-1}$  was recorded for the  $\text{Fe}_3\text{O}_4@\text{C}$  core–shell NP-based ferrofluid at the same concentration and temperature. The percentage enhancement was calculated using the following equation:

$$\text{Enhancement (\%)} = \frac{\sigma - \sigma_0}{\sigma_0} \times 100 \quad (2)$$

where  $\sigma_0$  = EC of DIW and  $\sigma$  = EC of the ferrofluid.

The maximum enhancement in the EC of the  $\text{Fe}_3\text{O}_4$  NP- and  $\text{Fe}_3\text{O}_4@\text{C}$  core–shell NP-based ferrofluids was obtained as  $\sim 3222\%$  and  $\sim 2015\%$ , respectively, for 0.7 vol% of NPs at 50 °C. There are many factors that affect the EC of a nanofluid or

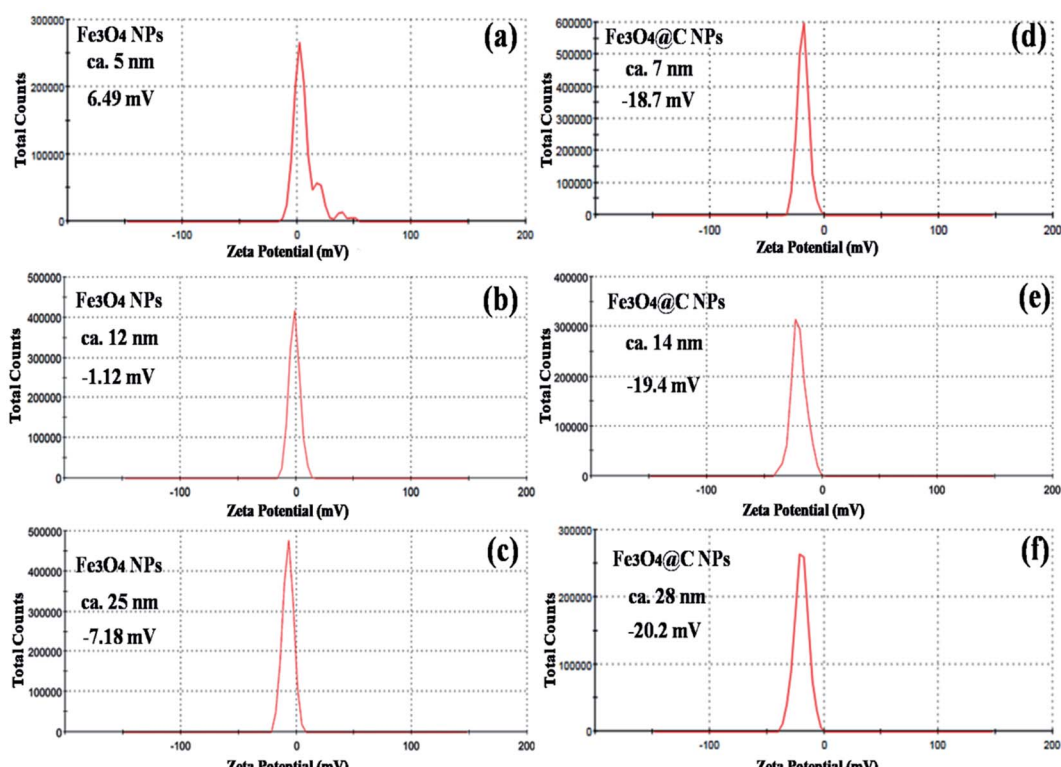


**Fig. 6** Zeta potential plots of (a) 5 nm  $\text{Fe}_3\text{O}_4$ , (b) 12 nm  $\text{Fe}_3\text{O}_4$ , (c) 25 nm  $\text{Fe}_3\text{O}_4$ , (d) 7 nm  $\text{Fe}_3\text{O}_4@\text{C}$ , (e) 14 nm  $\text{Fe}_3\text{O}_4@\text{C}$  and (f) 28 nm  $\text{Fe}_3\text{O}_4@\text{C}$  NP-based ferrofluids at 0.7 vol% NP concentration.



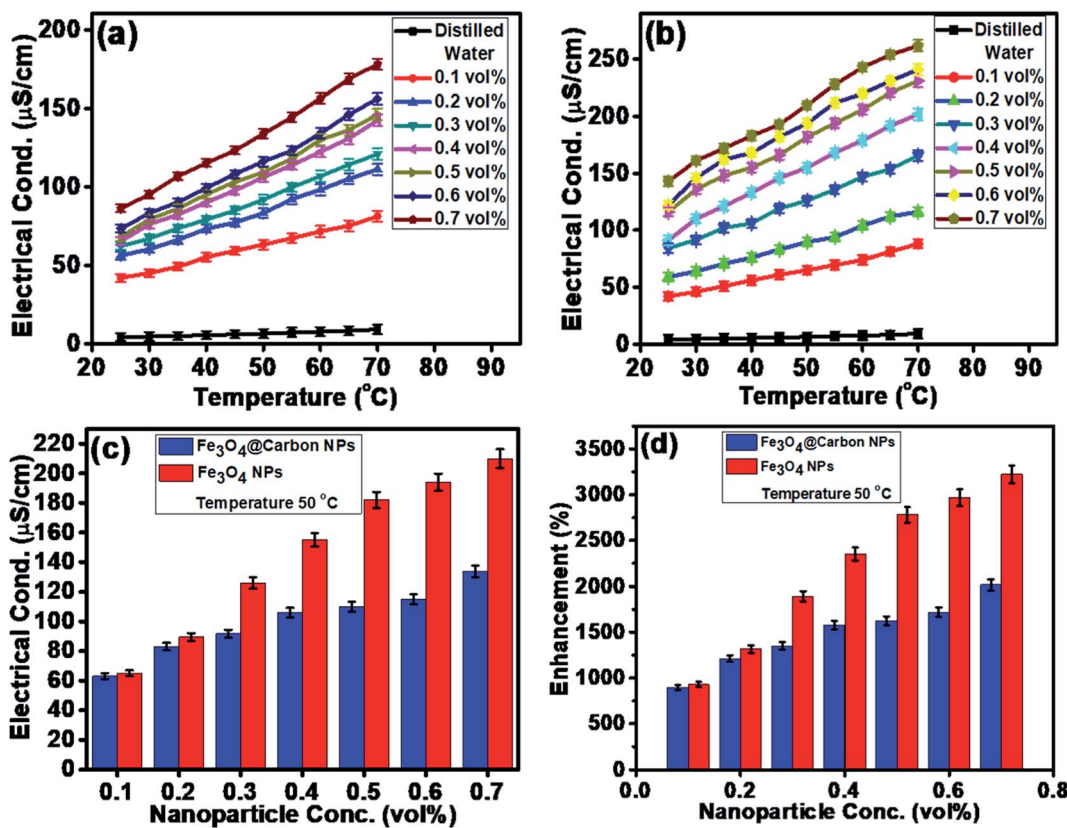


Fig. 7 Electrical conductivities of (a)  $\text{Fe}_3\text{O}_4$ @C NP (7 nm)-based ferrofluids and (b)  $\text{Fe}_3\text{O}_4$  NP (5 nm)-based ferrofluids at different temperatures. (c) Comparison of the electrical conductivities of the  $\text{Fe}_3\text{O}_4$  and  $\text{Fe}_3\text{O}_4$ @C core–shell NP-based ferrofluids at 50 °C and (d) Comparison of the percentage enhancement in electrical conductivity for the  $\text{Fe}_3\text{O}_4$  and  $\text{Fe}_3\text{O}_4$ @C core–shell NP-based ferrofluids at 50 °C with respect to DI water.

a ferrofluid such as volume fraction, temperature, structure of NPs, types of NPs, and types of fluids.<sup>60</sup> The EC of a nanofluid/ferrofluid generally increases with an increase in the volume fraction of the nanofluid/ferrofluid and with temperature. The ions on the surface of the colloidal NPs are attracted to the oppositely charged ions, which results in the formation of a layer. Another layer of ions is also formed, where the ions from the suspension become attached to the first layer by Coulomb force, which electrically screens the first layer. The ions in the second layer are loosely associated and move due to the electric force of attraction and thermal motion. Hence, as the temperature increases, the free ions move rapidly into the suspension of the ferrofluid, which results in a high EC. An increase in the concentration of NPs also enhanced the EC as more solid NPs suspended into the fluid were available to expose their surfaces toward the ions and formed an electrical double layer. However, a relatively low EC in the case of the  $\text{Fe}_3\text{O}_4$ @C core–shell NPs was observed as the carbon-coated suspended  $\text{Fe}_3\text{O}_4$  NPs had a lower number of electrons on their surfaces to get attracted toward the free ions compared to the bare  $\text{Fe}_3\text{O}_4$  NPs. The electrons were more populated near the Fermi level in the semiconductor ( $\text{Fe}_3\text{O}_4$ ) NPs compared to the non-metallic amorphous carbon. Hence, relatively low ECs were observed for the  $\text{Fe}_3\text{O}_4$ @C core–shell NP-based ferrofluids compared to the  $\text{Fe}_3\text{O}_4$  NP-based ferrofluids.

Similarly, the thermal conductivities of the  $\text{Fe}_3\text{O}_4$  NP- and  $\text{Fe}_3\text{O}_4$ @C core–shell NP-based ferrofluids were measured. Fig. 8a and b show the graphs of the coefficient of thermal conductivity *versus* temperature gradient for the  $\text{Fe}_3\text{O}_4$ @C core–shell NP (7 nm)- and  $\text{Fe}_3\text{O}_4$  NP (5 nm)-based ferrofluids, respectively. For both types of NPs, with concentrations in the range of 0.1 vol% to 0.7 vol%, it was observed that the coefficient of thermal conductivity ( $\lambda$ ) increased consistently. The average thermal conductivity coefficients for water was found to be  $0.71 \text{ W m}^{-1} \text{ K}^{-1}$ , and for the ferrofluids at different concentrations of  $\text{Fe}_3\text{O}_4$ @C core–shell NPs, *i.e.*, 0.1, 0.2, 0.3, 0.4, 0.5, 0.6 and 0.7 vol% they were found to be 0.82, 0.90, 0.99, 1.19, 1.22, 1.46 and  $1.54 \text{ W m}^{-1} \text{ K}^{-1}$ , respectively, as shown in Fig. 8a. A similar trend was observed for the  $\text{Fe}_3\text{O}_4$  NP-based ferrofluids, and the values of the coefficient of thermal conductivity for various concentrations, *i.e.*, 0.1, 0.2, 0.3, 0.4, 0.5, 0.6 and 0.7 vol% were obtained as 0.84, 0.92, 1.02, 1.16, 1.21, 1.48 and  $1.80 \text{ W m}^{-1} \text{ K}^{-1}$ , respectively, as shown in Fig. 8b. The comparison of thermal conductivities and percentage enhancement of  $\text{Fe}_3\text{O}_4$  NP- and  $\text{Fe}_3\text{O}_4$ @C core–shell NP-based ferrofluids are shown in Fig. 8c and d, respectively. Fig. 8d depicts the increase in percentage enhancement with respect to DI water from 16% to 116% as the concentration of  $\text{Fe}_3\text{O}_4$ @C core–shell NPs varied from 0.1 vol% to 0.7 vol%. Similarly, a 17% to 153% enhancement with respect to DI water was

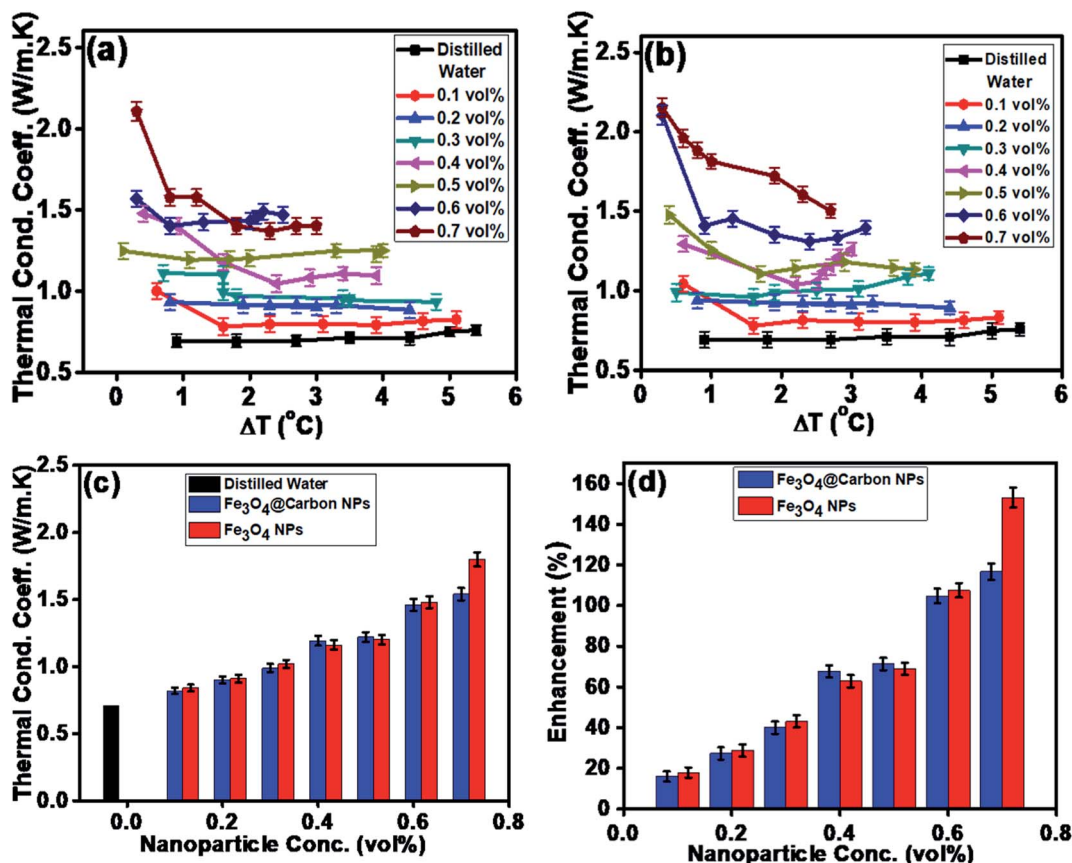


Fig. 8 Thermal conductivity with  $\Delta T$  (a)  $\text{Fe}_3\text{O}_4$ @C core–shell NP (7 nm)-based ferrofluids and (b)  $\text{Fe}_3\text{O}_4$  NP (5 nm)-based ferrofluids. (c) Comparative thermal conductivity coefficient and (d) comparative percent enhancement in thermal conductivity of  $\text{Fe}_3\text{O}_4$  NP- and  $\text{Fe}_3\text{O}_4$ @C core–shell NP-based ferrofluids with respect to DI water.

observed for the  $\text{Fe}_3\text{O}_4$  NPs as their concentration varied from 0.1 vol% to 0.7 vol%.

The maximum enhancement was observed for 0.7 vol% of  $\text{Fe}_3\text{O}_4$  NPs. This may be attributed to the clustering effect of the NPs as their surface energies were quite high owing to their high surface to volume ratio and the formation of a chain-like network of small-sized NPs, which increased the effective volume fraction of heat conductive phases in the ferrofluid.

Moreover, the dispersed NPs in the water-based ferrofluid executed Brownian motion, which led to collisions between the NPs and with the molecules of the water.<sup>61,62</sup> Conversely, in the case of the  $\text{Fe}_3\text{O}_4$ @C core–shell NPs, the thermal capacity of the carbon coating and percolation pathways for heat conduction were responsible for the thermal conductivity enhancement.<sup>61,62</sup> It should be noted that at only 0.7 vol%, the thermal conductivity of the  $\text{Fe}_3\text{O}_4$ @C core–shell NP-based ferrofluid was

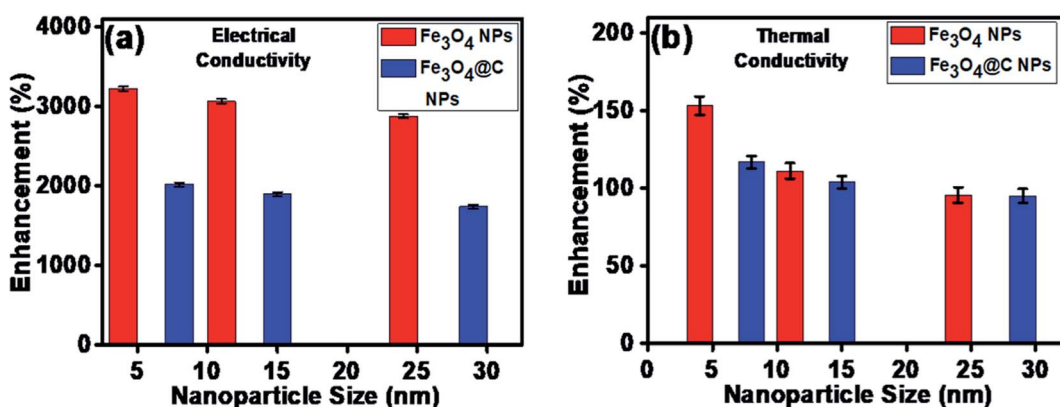


Fig. 9 Effect of NP size on (a) electrical conductivity enhancement and (b) thermal conductivity enhancement of ferrofluids.



significantly less than that of the  $\text{Fe}_3\text{O}_4$  NP-based ferrofluid. Moreover, the effects of different NPs sizes on the enhancement of the electrical and thermal conductivities were also studied, as shown in Fig. 9a and b (Fig. S2 and S3, ESI†), respectively. Fig. 9a shows the variation in the electrical conductivity enhancement of the  $\text{Fe}_3\text{O}_4$  NP- and  $\text{Fe}_3\text{O}_4@\text{C}$  NP-based ferrofluids with NP size. The EC was found to be enhanced with a decrease in the size of the NPs for both types of ferrofluids. The increase in EC with a decrease in the NP size is attributed to the increase in surface area and electrophoretic mobility of the NPs.<sup>63,64</sup> A similar trend was observed for the thermal conductivity enhancement, which increased with a decrease in NP size for both types of ferrofluids, as shown in Fig. 9b. The exceptional enhancement in the thermal conductivity especially in the case of the bare  $\text{Fe}_3\text{O}_4$  NP (5 nm)-based ferrofluid compared

to the larger-size  $\text{Fe}_3\text{O}_4$  NP (12 nm and 25 nm)-based ferrofluids is due to the more pronounced effect of chain-like network formation/clustering of the NPs, as inferred from the zeta potential values (Table 1 and Fig. 6). However, owing to the carbon coating over the bare  $\text{Fe}_3\text{O}_4$  NPs, relatively better dispersion and less agglomeration of the different sized  $\text{Fe}_3\text{O}_4@\text{C}$  NPs (as inferred from their more negative zeta potential values, Table 1 and Fig. 6) in the base fluid (water) resulted in a lower enhancement in thermal conductivity for the  $\text{Fe}_3\text{O}_4@\text{C}$  NP-based ferrofluids compared to the  $\text{Fe}_3\text{O}_4$  NP-based ferrofluids.

To theoretically validate the obtained results, the experimental values of the thermal conductivities of the  $\text{Fe}_3\text{O}_4$  NP (*ca.* 5 nm)- and  $\text{Fe}_3\text{O}_4@\text{C}$  NP (*ca.* 7 nm)-based ferrofluids were fitted with the existing Maxwell model,<sup>65</sup> as shown in Fig. 10. Based on the effective medium theory, the effective thermal conductivity of the  $\text{Fe}_3\text{O}_4$  NPs coated with carbon was calculated using the following equation:<sup>66</sup>

$$k_{\text{ep}} = \frac{[2(1 - \gamma) + (1 + \beta)^3(1 + 2\gamma)]\gamma}{-(1 - \gamma) + (1 + \beta)^3(1 + 2\gamma)} k_p \quad (3)$$

where  $k_{\text{ep}}$  is the equivalent thermal conductivity of the  $\text{Fe}_3\text{O}_4@\text{C}$  NPs,  $k_p$  is the thermal conductivity of the  $\text{Fe}_3\text{O}_4$  NPs,  $\gamma$  is the ratio of coated nanolayer thermal conductivity to the particle thermal conductivity, and  $\beta$  is the ratio of coated layer thickness to that of the particle radius. The thermal conductivity of the ferrofluids based on  $\text{Fe}_3\text{O}_4$  NPs and  $\text{Fe}_3\text{O}_4@\text{C}$  NPs was calculated using the Maxwell equation as follows:

$$\frac{k_{\text{ff}}}{k_{\text{bf}}} = \frac{k_{\text{np}} + 2k_{\text{pf}} - 2\mathcal{O}_{\text{np}}(k_{\text{bf}} - K_{\text{np}})}{k_{\text{np}} + 2k_{\text{bf}} + \mathcal{O}_{\text{np}}(k_{\text{bf}} - K_{\text{np}})} \quad (4)$$

where  $k_{\text{ff}}$ ,  $k_{\text{bf}}$  and  $k_{\text{np}}$  are thermal conductivities of the ferrofluid, base fluid and NP ( $k_{\text{ep}}$  was used instead of  $k_{\text{np}}$  in the case of the carbon-coated  $\text{Fe}_3\text{O}_4$  NPs), respectively, and  $\mathcal{O}_{\text{np}}$  is the

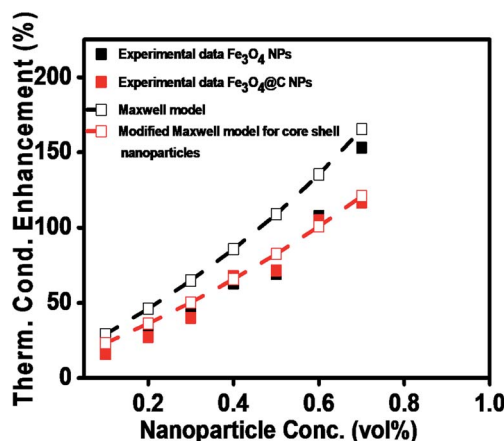


Fig. 10 Comparison of experimental and predicted values of thermal conductivities of  $\text{Fe}_3\text{O}_4$  (*ca.* 5 nm) and  $\text{Fe}_3\text{O}_4@\text{C}$  (*ca.* 7 nm) NP-based ferrofluids.

Table 2 Comparison of the electrical and thermal conductivities of our  $\text{Fe}_3\text{O}_4$  and  $\text{Fe}_3\text{O}_4@\text{C}$  core–shell NP-based ferrofluids with that in the literature

Material	Size (nm)	Conc./volume fraction	Base fluid	Electrical conductivity enhancement (%)	Thermal conductivity enhancement (%)	Ref.
$\text{Fe}_3\text{O}_4$	14.2	0.5	Water	360	—	68
$\text{SiO}_2$	12	1.1–2.4	Water	—	1.1	69
$\text{TiO}_2$	27	3.1–4.3			10.8	
$\text{Al}_2\text{O}_3$	13	1.3–4.3			32.4	
Graphene	—	0.5/0.1	Ethylene glycol/water	1664	10.47	70
$\text{Fe}@\text{C}$	—	1.5 wt%	Polyethylene glycol	—	30	39
$\text{Al}@\text{C}$					40	
$\text{Cu}@\text{C}$					49	
Iron oxide(n,m)	50	$1 \text{ g L}^{-1}$	Water	—	34	34
$\text{Fe}_3\text{O}_4$	5–10	$2.5 \text{ g L}^{-1}$	Mineral oil	—	51	19
$\gamma\text{-Fe}_2\text{O}_3$	12	$1.5 \text{ g L}^{-1}$	50 : 50 oil mixture	—	51	21
$\text{CuO}$	29	0–6	Ethylene glycol/water	—	60	71
$\text{Al}_2\text{O}_3$	53	0–10			69	
$\gamma\text{-Fe}_2\text{O}_3$	13	$1.5 \text{ g L}^{-1}$	Liquid paraffin/sunflower/mineral oil	—	20.6	20
					45.2	
					77	
$\text{Fe}_3\text{O}_4@\text{C}$	7	0.7 vol%	Water	2015	116	This work
$\text{Fe}_3\text{O}_4$ NPs	5			3222	153	



concentration of NPs (vol%) in the base fluid. It can be seen in Fig. 10 that the values predicted by the Maxwell model are higher at low concentrations for the  $\text{Fe}_3\text{O}_4$  NP (*ca.* 5 nm)-based ferrofluids. In contrast, for the  $\text{Fe}_3\text{O}_4@\text{C}$  (*ca.* 7 nm) NP-based ferrofluid, the predicted values of thermal conductivity closely fit the experimental data. The slight deviation in the thermal conductivity values of the  $\text{Fe}_3\text{O}_4$  NP-based ferrofluids is attributed to the clustering or aggregation of the NPs, as inferred from the zeta potential values (Table 1 and Fig. 6).<sup>67</sup> Therefore, the Maxwell model validated the experimental results for the  $\text{Fe}_3\text{O}_4@\text{C}$  NP-based ferrofluid. These obtained results were compared with the results reported in the literature, as presented in Table 2.

## 4. Conclusion

In conclusion,  $\text{Fe}_3\text{O}_4$  and  $\text{Fe}_3\text{O}_4@\text{C}$  core–shell NP-based ferrofluids were prepared to investigate their thermal and electrical conductivities. Firstly, we synthesized different sized  $\text{Fe}_3\text{O}_4$  NPs *via* a chemical co-precipitation method using iron salts and alkali solution as precursors. The successfully synthesized  $\text{Fe}_3\text{O}_4$  NPs were introduced in an autoclave with a solution of glucose at 180 °C and high pressure. The hydrothermal process enabled the formation of a carbon shell over the  $\text{Fe}_3\text{O}_4$  NPs. The average particle sizes of the  $\text{Fe}_3\text{O}_4$  and  $\text{Fe}_3\text{O}_4@\text{C}$  core–shell NPs were found to be in the range of 5–25 nm and 7–28 nm, respectively. The structural and elemental analyses revealed that no phase transformation of  $\text{Fe}_3\text{O}_4$  occurred during the formation of core–shell NPs. The magnetic characterization revealed that the as-synthesized small average-sized  $\text{Fe}_3\text{O}_4$  NPs (*ca.* 5 nm) and  $\text{Fe}_3\text{O}_4@\text{C}$  core–shell NPs (*ca.* 7 nm) were superparamagnetic in nature. Finally, the electrical and thermal conductivities of the  $\text{Fe}_3\text{O}_4$  and  $\text{Fe}_3\text{O}_4@\text{C}$  core–shell NP-based ferrofluids were measured at different concentrations of NPs and with different sized NPs. Exceptional results were obtained, where the electrical conductivity was enhanced up to  $\sim 3222\%$  and  $\sim 2015\%$  for the  $\text{Fe}_3\text{O}_4$  (*ca.* 5 nm) and  $\text{Fe}_3\text{O}_4@\text{C}$  (*ca.* 7 nm) core–shell NP-based ferrofluids, respectively, compared to distilled water (base fluid). Similarly, the enhancement in the thermal conductivity was determined to be  $\sim 153\%$  and  $\sim 116\%$  for the  $\text{Fe}_3\text{O}_4$  (*ca.* 5 nm) and  $\text{Fe}_3\text{O}_4@\text{C}$  (*ca.* 7 nm) core–shell NPs, respectively.

## Author contributions

Mohd Imran: Conceptualization, methodology, investigation, writing—original draft preparation, supervision; Nasser Zouli: visualization, investigation, supervision; Tansir Ahamad: characterization, investigation, funding; Saad M. Alshehri: characterization, investigation, funding; Mohammed Rehaan Chandan: visualization, validation, review & editing; Shahir Hussain: conceptualization, methodology, investigation, electrical conductivity experiment; Abdul Aziz: resources, thermal conductivity experiment; Mushtaq Ahmad Dar: data curation, characterization; Afzal Khan: visualization investigation, supervision, review & editing.

## Conflicts of interest

The authors declare no competing financial interest.

## Acknowledgements

The authors gratefully acknowledge the Deanship of Scientific Research at King Saud University for funding this project (RG-1438-026). The authors are also grateful to King Saud University, Riyadh, and Jazan University, Jazan, Kingdom of Saudi Arabia for providing experimental facilities.

## References

- 1 W. H. Azmi, K. V. Sharma, R. Mamat, G. Najafi and M. S. Mohamad, The Enhancement of Effective Thermal Conductivity and Effective Dynamic Viscosity of Nanofluids—A Review, *Renewable Sustainable Energy Rev.*, 2016, **53**, 1046–1058.
- 2 A. Gandomkar, M. H. Saidi, M. B. Shafii, M. Vandadi and K. Kalan, Visualization and Comparative Investigations of Pulsating Ferro-Fluid Heat, *Appl. Therm. Eng.*, 2017, **116**, 56–65.
- 3 M. A. Nazari, M. H. Ahmadi, R. Ghasempour, M. B. Shafii, O. Mahian, S. Kalogirou, *et al.*, A Review on Pulsating Heat Pipes: From Solar to Cryogenic Applications, *Appl. Energy*, 2018, **222**, 475–484.
- 4 M. A. Nazari, M. H. Ahmadi, R. Ghasempour and M. B. Shafii, How to Improve the Thermal Performance of Pulsating Heat Pipes: A Review on Working Fluid, *Renewable Sustainable Energy Rev.*, 2018, **91**, 630–638.
- 5 A. Baghban, F. Pourfayaz, M. H. Ahmadi, A. Kasaian, S. M. Pourkiaei and G. Lorenzini, *et al.*, Connectionist Intelligent Model Estimates of Convective Heat Transfer Coefficient of Nanofluids in Circular Cross-Sectional Channels, *J. Therm. Anal. Calorim.*, 2018, **132**, 1213–1239.
- 6 M. M. Tawfik, Experimental Studies of Nanofluid Thermal Conductivity Enhancement and Applications: A Review, *Renewable Sustainable Energy Rev.*, 2017, **75**, 1239–1253.
- 7 S. Ponmani, J. K. M. William, R. Samuel, R. Nagarajan and J. S. Sangwai, Formation and Characterization of Thermal and Electrical Properties of CuO and ZnO Nanofluids in Xanthan Gum, *Colloids Surf. A*, 2014, **443**, 37–43.
- 8 O. A. Alawi, N. A. C. Sidik, H. W. Xian, T. H. Kean and S. N. Kazi, Thermal Conductivity and Viscosity Models of Metallic Oxides Nanofluids, *Int. J. Heat Mass Transfer*, 2018, **116**, 1314–1325.
- 9 W. Cui, Z. Shen, J. Yang and S. Wu, Molecular Dynamics Simulation on Flow Behaviors of Nanofluids Confined in Nanochannel, *Case Stud. Therm. Eng.*, 2015, **5**, 114–121.
- 10 T. K. Hong, H. S. Yang and C. J. Choi, Study of the Enhanced Thermal Conductivity of Fe Nanofluids, *J. Appl. Phys.*, 2005, **97**, 064311.
- 11 J. Garg, B. Poudel, M. Chiesa, J. B. Gordon, J. J. Ma, J. Garg, *et al.*, Enhanced Thermal Conductivity and Viscosity of Copper Nanoparticles in Ethylene Glycol Nanofluid, *J. Appl. Phys.*, 2008, **103**, 074301.



12 H. Zhang, Q. Wu, J. Lin, J. Chen, Z. Xu, H. Zhang, *et al.*, Thermal Conductivity of Polyethylene Glycol Nanofluids Containing Carbon Coated Metal Nanoparticles, *J. Appl. Phys.*, 2010, **108**, 124304.

13 M. Javed, A. H. Shaik, T. A. Khan, M. Imran, A. Aziz and A. R. Ansari, *et al.* Synthesis of Stable Waste Palm Oil Based CuO Nanofluid for Heat Transfer Applications, *Heat Mass Transfer*, 2018, 1–7.

14 D. Maity and D. C. Agrawal, Synthesis of Iron Oxide Nanoparticles Under Oxidizing Environment and Their Stabilization in Aqueous and Non-Aqueous Media, *J. Magn. Magn. Mater.*, 2007, **308**, 46–55.

15 Y. Wang, C. Wang, Z. Zhang and K. Xiao, Effect of Nanoparticles on the Morphology, Thermal, and Electrical Properties of Low Density Polyethylene After Thermal Aging, *Nanomaterials*, 2017, **7**(10), 320.

16 D. Guo, G. Xie and J. Luo, Mechanical Properties of Nanoparticles: Basics and Applications, *J. Phys. D: Appl. Phys.*, 2014, **47**, 013001.

17 K. L. Kelly, E. Coronado, L. L. Zhao and G. C. Schatz, The Optical Properties of Metal Nanoparticles: The Influence of Size, Shape, and Dielectric Environment, *J. Phys. Chem. B*, 2003, **107**(3), 668–677.

18 R. Sharma, V. V. Agrawal, A. K. Srivastava, L. Nain, M. Imran and S. R. Kabi, *et al.* Phase Control of Nanostructured Iron Oxide for Application to Biosensor, *J. Mater. Chem. B*, 2013, **14**, 464–474.

19 M. Imran, A. R. Ansari, A. H. Shaik, S. Hussain, A. Khan and M. R. Chandan, Ferrofluid Synthesis Using Oleic Acid Coated  $\text{Fe}_3\text{O}_4$  Nanoparticles Dispersed in Mineral Oil for Heat Transfer Applications, *Mater. Res. Express*, 2018, **5**(3), 036108.

20 M. Imran, A. H. Shaik, A. R. Ansari, A. Aziz, S. Hussain, A. F. Fadil Abouatiaa, A. Khan and M. R. Chandan, Synthesis of Highly Stable  $\gamma\text{-Fe}_2\text{O}_3$  Ferrofluid Dispersed in Liquid Paraffin, Motor Oil and Sunflower Oil for Heat Transfer Applications, *RSC Adv.*, 2018, **8**(25), 13970–13975.

21 A. A. Abutaleb, Effect of the Mixture of Mineral/Sunflower Oil Based Ferrofluid on Thermal and Flow Properties, *Mater. Res. Express*, 2019, **6**(4), 046101.

22 M. Imran, A. Abutaleb, M. A. Ali, T. Ahamad, A. R. Ansari, M. Shariq, D. Lolla and A. Khan, UV Light Enabled Photocatalytic Activity of  $\alpha\text{-Fe}_2\text{O}_3$  Nanoparticles Synthesized *via* Phase Transformation, *Mater. Lett.*, 2020, **258**, 126748.

23 S. Xuan, L. Hao, W. Jiang, X. Gong, Y. Hu and Z. Chen, A Facile Method to Fabricate Carbon-Encapsulated  $\text{Fe}_3\text{O}_4$  Core/Shell Composites, *Nanotech*, 2007, **18**, 035602.

24 L. Wang, K. Lin, J. Ren, K. Du, Y. Chang, L. Han, P. Yao and F. Tian, Direct Synthesis of Ultra Small and Stable Magnetite Nanoparticles Coated with One Single Carbon Layer for Sensitive Surface-Enhanced Raman Scattering, *Appl. Surf. Sci.*, 2019, **478**, 601–606.

25 C. He, S. Wu, N. Zhao, C. Shi, E. Liu and J. Li, Carbon-Encapsulated  $\text{Fe}_3\text{O}_4$  Nanoparticles as a High-Rate Lithium Ion Battery Anode Material, *ACS Nano*, 2013, **7**(5), 4459–4469.

26 N. Zhao, S. Wu, C. He, Z. Wang, C. Shi, E. Liu and J. Li, One-Pot Synthesis of Uniform  $\text{Fe}_3\text{O}_4$  Nanocrystals Encapsulated in Interconnected Carbon Nanospheres for Superior Lithium Storage Capability, *Carbon*, 2013, **57**, 130–138.

27 C. H. Liang, C. C. Wang, Y. C. Lin, C. H. Chen, C. H. Wong and C. Y. Wu, Iron Oxide/Gold Core/Shell Nanoparticles for Ultrasensitive Detection of Carbohydrate–Protein Interactions, *Anal. Chem.*, 2009, **81**(18), 7750–7756.

28 W. W. Xian, G. X. Zhu, C. J. Xia and Y. Ye, A Solution Phase Fabrication of Magnetic Nanoparticles Encapsulated in Carbon, *Nanotech*, 2006, **17**(17), 4307.

29 J. Li and C. Y. Liu, Carbon-Coated Copper Nanoparticles: Synthesis, Characterization and Optical Properties, *New J. Chem.*, 2009, **33**(7), 1474–1477.

30 X. Sun and Y. Li, Ag@C Core/Shell Structured Nanoparticles: Controlled Synthesis, Characterization, and Assembly, *Langmuir*, 2005, **21**(13), 6019–6024.

31 E. E. Carpenter, S. Calvin, R. M. Stroud and V. G. Harris, Passivated Iron as Core–Shell Nanoparticles, *Chem. Mater.*, 2003, **15**(17), 3245–3246.

32 W. L. Zhou, E. E. Carpenter, J. Lin, A. Kumbhar, J. Sims and C. J. O'Connor, Nanostructures of Gold Coated Iron Core–Shell Nanoparticles and the Nanobands Assembled Under Magnetic Field, *Eur. Phys. J. D*, 2001, **16**(1), 289–292.

33 H. Cui and D. Li, Fabrication and Properties Research on a Novel Perfluoropolyether Based Ferrofluid, *J. Magn. Magn. Mater.*, 2019, **473**, 341–347.

34 J. Zupan and M. M. Renjo, Thermal and Rheological Properties of Water-Based Ferrofluids and Their Applicability as Quenching Media, *Phys. Procedia*, 2015, **75**, 1458–1467.

35 A. Gavili, F. Zabihi, T. D. Isfahani and J. Sabbaghzadeh, The Thermal Conductivity of Water Base Ferrofluids Under Magnetic Field, *Exp. Therm. Fluid Sci.*, 2012, **41**, 94–98.

36 S. Dutz, J. H. Clement, D. Eberbeck, T. Gelbrich, R. Hergt, R. Müller, *et al.*, Ferrofluids of Magnetic Multicore Nanoparticles for Biomedical Applications, *J. Magn. Magn. Mater.*, 2009, **321**(10), 1501–1504.

37 V. M. Wu, E. Huynh, S. Tang and V. Uskoković, Brain and Bone Cancer Targeting by a Ferrofluid Composed of Superparamagnetic Iron-Oxide/Silica/Carbon Nanoparticles, *Actabiomater*, 2019, **88**, 422–447.

38 G. Kandasamy, A. Sudame, D. Maity, S. Soni, K. Sushmita, N. S. Veerapu, *et al.*, Multifunctional Magnetic-Polymeric Nanoparticles Based Ferrofluids for Multi-Modal *in Vitro* Cancer Treatment Using Thermotherapy and Chemotherapy, *J. Mol. Liq.*, 2019, **293**, 111549.

39 A. Kaushik, J. Rodriguez, D. Rothen, V. Bhardwaj, R. D. Jayant, P. Pattany, B. Fuentes, *et al.*, MRI-guided, Non-invasive Delivery of Magneto-electric Drug Nanocarriers to the Brain in a Nonhuman Primate, *ACS Appl. Bio Mater.*, 2019, **2**, 4826–4836.

40 P. Pandey, G. Ghimire, J. Garcia, A. Rubfiaro, X. Wang, A. Tomitaka, M. Nair, A. Kaushik and J. He, Single-entity Approach to Investigate Surface Charge Enhancement in



Magnetoelectric Nanoparticles Induced by AC Magnetic Field Stimulation, *ACS Sens.*, 2020, DOI: 10.1021/acssensors.0c00664.

41 A. Tomitaka, A. Kaushik, B. D. Kevadiya, I. Mukadam, H. E. Gendelman, K. Khalili, G. Liu and M. Nair, Surface-engineered Multimodal Magnetic Nanoparticles to Manage CNS Diseases, *Drug Discovery Today*, 2019, **24**, 873–882.

42 A. Kaushik, R. N. Moshai, R. Sinha, V. Bhardwaj, V. Atluri, R. D. Jayant, A. Yndart, B. Kateb, N. Pala and M. Nair, Investigation of AC-Magnetic Field Stimulated Nanoelectroporation of Magneto-electric Nano-drug-carrier Inside CNS Cells, *Sci. Rep.*, 2017, **7**, 1–12.

43 A. Kaushik, A. Yndart, V. Atluri, S. Tiwari, A. Tomitaka, P. Gupta, R. D. Jayant, D. A. Carbonell, K. Khalili and M. Nair, Magnetically Guided Non-invasive CRISPR-Cas9/gRNA Delivery Across Blood-brain Barrier to Eradicate Latent HIV-1 Infection, *Sci. Rep.*, 2019, **9**, 1–11.

44 K. V. Chandekar, M. Shkir, T. Alshahrani, E. H. Ibrahim, M. Kilany, Z. Ahmad, M. A. Manthrammel, S. AlFaify, B. Kateb and A. Kaushik, One-spot Fabrication and In-vivo Toxicity Evaluation of Core-shell Magnetic Nanoparticles, *Mater. Sci. Eng., C*, 2021, 111898.

45 R. Kumar, K. Mondal, P. K. Panda, A. Kaushik, R. Abolhassani, R. Ahuja, H. G. Rubahn and Y. K. Mishra, Core-shell Nanostructures: Perspectives Towards Drug Delivery Applications, *J. Mater. Chem. B*, 2020, **8**, 8992–9027.

46 M. Imran, A. A. A. Ahmed, B. Kateb and A. Kaushik, Inorganic Nanostructures for Brain Tumor Management, in *Nanotherapy for Brain Tumor Drug Delivery*, Humana, New York, 2021, pp. 145–178.

47 H. Zhang, Q. Wu, J. Lin, J. Chen and Z. Xu, Thermal Conductivity of Polyethylene Glycol Nanofluids Containing Carbon Coated Metal Nanoparticles, *J. Appl. Phys.*, 2010, **108**(12), 124304.

48 T. T. Baby and R. Sundara, Surfactant Free Magnetic Nanofluids Based on Core-shell Type Nanoparticle Decorated Multiwalled Carbon Nanotubes, *J. Appl. Phys.*, 2011, **110**(6), 064325.

49 D. Fan, Q. Li, W. Chen and J. Zeng, Graphene Nanofluids Containing Core-Shell Nanoparticles with Plasmon Resonance Effect Enhanced Solar Energy Absorption, *Sol. Energy*, 2017, **158**, 1–8.

50 R. Islam and B. Shabani, Prediction of Electrical Conductivity of  $TiO_2$  Water and Ethylene Glycol-Based Nanofluids for Cooling Application in Low Temperature PEM Fuel Cells, *Energy Procedia*, 2019, **160**, 550–557.

51 G. Zhao, J. J. Feng, Q. L. Zhang, S. P. Li and H. Y. Chen, Synthesis and Characterization of Prussian Blue Modified Magnetite Nanoparticles and Its Application to the Electrocatalytic Reduction of  $H_2O_2$ , *Chem. Mater.*, 2005, **17**(12), 3154–3159.

52 K. Tao, H. Dou and K. Sun, Facile Interfacial Co-Precipitation to Fabricate Hydrophilic Amine-Capped Magnetite Nanoparticles, *Chem. Mater.*, 2006, **18**(22), 5273–5278.

53 M. I. Dar and S. A. Shivashankar, Single Crystalline Magnetite, Maghemite, and Hematite Nanoparticles with Rich Coercivity, *RSC Adv.*, 2014, **4**(8), 4105–4113.

54 D. Ağaoğulları, S. J. Madsen, B. Öğüt, A. L. Koh and R. Sinclair, Synthesis and Characterization of Graphite-Encapsulated Iron Nanoparticles From Ball Milling-Assisted Low-Pressure Chemical Vapor Deposition, *Carbon*, 2017, **124**, 170–179.

55 H. Hu, Y. Yuan, S. Lim and C. H. Wang, Phase Structure Dependence of Magnetic Behaviour in Iron Oxide Nanorods, *Mater. Des.*, 2020, **185**, 108241.

56 M. L. O. Pereira, K. C. B. Maia, W. C. Silva, A. C. Leite, A. D. S. Francisco, T. L. Vasconcelos, R. S. V. Nascimento and D. Grasseschi,  $Fe_3O_4$  Nanoparticles as Surfactant Carriers for Enhanced Oil Recovery and Scale Prevention, *ACS Appl. Nano Mater.*, 2020, **3**(6), 5762–5772.

57 S. Wu, D. Zhu, X. Li, H. Li and J. Lei, Thermal Energy Storage Behavior of  $Al_2O_3$ – $H_2O$  Nanofluids, *Thermochim. Acta*, 2009, **483**, 73–77.

58 X. Q. Xu, H. Shen, J. R. Xu, M. Q. Xie and X. J. Li, The Colloidal Stability and Core-Shell Structure of Magnetite Nanoparticles Coated with Alginate, *Appl. Surf. Sci.*, 2006, **253**(4), 2158–2164.

59 G. Kandasamy, A. Sudame, T. Luthra, K. Saini and D. Maity, Functionalized Hydrophilic Superparamagnetic Iron Oxide Nanoparticles for Magnetic Fluid Hyperthermia Application in Liver Cancer Treatment, *ACS Omega*, 2018, **3**, 3991–4005.

60 J. Philip, P. D. Shima and B. Raj, Enhancement of Thermal Conductivity in Magnetite Based Nanofluid Due to Chain Like Structures, *Appl. Phys. Lett.*, 2007, **91**, 203108.

61 P. Kebbinski, S. R. Phillipot, S. U. S. Choi and J. A. Eastman, Mechanisms of Heat Flow in Suspensions of Nano-Sized Particles, *Int. J. Heat Mass Transfer*, 2002, **45**(4), 855–863.

62 S. Bagheli, H. K. Fadafan, R. L. Orimi and M. Ghaemi, Synthesis and Experimental Investigation of the Electrical Conductivity of Water Based Magnetite Nanofluids, *Powder Technol.*, 2015, **274**, 426–430.

63 K. K. Sarojini, S. V. Manoj, P. K. Singh, T. Pradeep and S. K. Das, Electrical Conductivity of Ceramic and Metallic Nanofluids, *Colloids Surf., A*, 2013, **417**, 39–46.

64 H. Konakanchi, R. Vajjha, D. Misra and D. Das, Electrical Conductivity Measurements of Nanofluids and Development of New Correlations, *J. Nanosci. Nanotechnol.*, 2011, **11**, 6788–6795.

65 J. C. Maxwell, *A Treatise on Electricity and Magnetism*, Dover Publications, New York, 1954.

66 L. M. Schwartz, E. J. Garboczi and D. P. Bentz, Interfacial Transport in Porous Media: Application to DC Electrical Conductivity of Mortars, *J. Appl. Phys.*, 1995, **78**(10), 5898–5908.

67 C. Kleinstreuer and Y. Feng, Experimental and Theoretical Studies of Nanofluid Thermal Conductivity Enhancement: A Review, *Nanoscale Res. Lett.*, 2011, **6**, 229.

68 H. Masuda, A. Ebata, K. Teramae, N. Hishinuma and Y. Ebata, Alteration of Thermal Conductivity and Viscosity



of Liquid by Dispersing Ultra-Fine Particles, *Netsu Bussei*, 1993, **7**(4), 227–233.

69 A. Ijam, R. Saidur, P. Ganesan and A. M. Golsheikh, Stability, Thermo-Physical Properties, and Electrical Conductivity of Graphene Oxide-Deionized Water/Ethylene Glycol Based Nanofluid, *Int. J. Heat Mass Transfer*, 2015, **87**, 92–103.

70 R. S. Vajjha and D. K. Das, Experimental Determination of Thermal Conductivity of Three Nanofluids and Development of New Correlations, *Int. J. Heat Mass Transfer*, 2009, **52**, 4675–4682.

71 Y. Geng, H. Khodadadi, A. Karimipour, M. R. Safaei and T. K. Nguyen, A Comprehensive Presentation on Nanoparticles Electrical Conductivity of Nanofluids: Statistical Study Concerned Effects of Temperature, Nanoparticles Type and Solid Volume Concentration, *Phys. A*, 2019, 123432.

